Distinct Mechanisms for Inhibition of SARS-CoV-2 Main Protease: Dimerization Promoted by Peptidomimetic Inhibitors and Disrupted by Ebselen

Chengxi Liu,[1,2,#] Qinyu Jia,[1,2,#] Chang Zhao,[1,2,#] Zhong-Ping Yao[1,2,*]

[1]Department of Applied Biology and Chemical Technology, Food Safety and Technology Research Centre, and Research Centre for Chinese Medicine Innovation, The Hong Kong Polytechnic University, Hung Hom, Kowloon, Hong Kong SAR, China

[2]State Key Laboratory of Chinese Medicine and Molecular Pharmacology (Incubation), and Shenzhen Key Laboratory of Food Biological Safety Control, Hong Kong Polytechnic University Shenzhen Research Institute, Shenzhen 518057, China

[#]These authors contributed to the work equally.

*Correspondence: zhongping.yao@polyu.edu.hk

Abstract

The SARS-CoV-2 main protease (M^{pro}) is a key target for antiviral drugs. Given its conserved sequence across coronaviruses and its essential role in viral replication, numerous inhibitors have been developed to target its active site. M^{pro} exists in equilibrium between the active dimer and inactive monomer, rendering the targeting of dimerization as a promising alternative strategy for drug development. This study addresses knowledge gaps regarding the monomer-dimer equilibrium and conformational changes of M^{pro} induced by inhibitor binding. We utilized ^{13}C labeling combined with native mass spectrometry to assess how different types of inhibitors (including peptidomimetic inhibitors PF-07321332, PF-00835231, GC376, boceprevir; non-peptidomimetic inhibitors carmofur, ebselen and its analog MR6-31-2; and allosteric inhibitors AT7519 and pelitinib) influence the monomer-dimer equilibrium and subunit exchange of M^{pro}. Additionally, we employed hydrogen/deuterium exchange mass spectrometry (HDX-MS) to investigate the conformational dynamics of M^{pro} and its interactions with these inhibitors. Key findings revealed divergent mechanisms: peptidomimetic inhibitors significantly shifted the equilibrium towards the dimeric state, suppressing subunit exchange dynamics and rigidifying the dimer interface. In contrast, ebselen impaired the dimer form and increased the flexibility of the dimer interface. Notably, we identified a novel covalent binding site for ebselen at C300 by tandem mass spectrometry, with molecular dynamics simulations further indicating that this modification allosterically altered the hydrogen bond network of the M^{pro} dimer interface. Overall, this study reveals distinct inhibitory modes between peptidomimetic inhibitors and ebselen, highlighting the potential of targeting allosteric sites at the dimer interface for the design of next-generation M^{pro} inhibitors.

Introduction

Severe acute respiratory syndrome coronavirus 2 (SARS-CoV-2), the causative agent of COVID-19, caused global infections, fatalities, and profound socioeconomic disruptions (Zhu et al., 2020). SARS-CoV-2 contains a ~30 kb single-stranded RNA, which includes the ORF1ab gene that encodes two large overlapping polyprotein precursors (pp1a and pp1ab) (Zhang et al., 2020). The cleavage of the two inactive polyproteins into 16 individual active nonstructural proteins is essential for viral replication and proliferation. This cleavage process is performed by two viral proteases: the papain-like protease and the main protease (M^{pro}). M^{pro} is a cysteine protease produced by autolytic cleavage from pp1a and pp1ab and is responsible for the generation of 12 nonstructural proteins from the two polyproteins (Yang et al., 2003). M^{pro} exhibits a highly conserved three-dimensional structure among various coronaviruses, e.g., SARS-CoV-2, SARS-CoV, MERS-CoV, and BAT-CoV (Goyal and Goyal, 2020), offering the potential for broad-spectrum anti-coronaviral drug development.

M^{pro} is a homodimeric protein, with each monomer consisting of three domains. Domain I (residues 10-99) and Domain II (residues 100-182) feature an antiparallel β-barrel structure, and Domain III (residues 198-303) contains five α-helices connected to Domain II by a long linker loop (residues 183-197) (Jin et al., 2020a). The substrate-binding site (active site), located in a cleft between Domain I and Domain II, has been defined into four subsites (S1, S2, S4 and S1'), which contain a histidine/cysteine catalytic dyad: H41 and C145 (Figure 1a). SARS-CoV-2 M^{pro} is in an equilibrium between the active dimer and inactive monomer in solution. Dimerization is essential for the M^{pro} to perform enzymatic activity, with key dimer interface residues playing a critical role in shaping the structure of the active site pocket. The dimer interface includes the N-finger (residues 1-7), residues 121-129, residues 132-142, R298 and Q299 (Gao et al., 2023). In the dimer structure, the N-finger of one monomer is

squeezed between Domain II and Domain III of the other monomer. This allows residues S1 and R4 of one M^{pro} monomer to interact with E166 and E290 of the other monomer, respectively, adjusting the orientation of the S1 pocket of the active site for substrate binding (Sacco et al., 2020). R4A and E290A were previously reported to eliminate activity for SARS-CoV M^{pro} (Chou et al., 2004). Similarly, M^{pro} carrying E166A showed markedly lower enzymatic activity (Jochmans et al., 2023).

Various M^{pro} inhibitors have been developed to target M^{pro}, primarily by repurposing clinically approved drugs or adapting inhibitors originally designed against SARS-CoV M^{pro} (Hoffman et al., 2020; Yang and Yang, 2021). Among these, many inhibitors are peptidomimetic compounds that covalently bind to C145 within the active site, such as PF-07321332, PF-00835231, GC376, and boceprevir. PF-07321332 (nirmatrelvir) is the first orally administered inhibitor targeting SARS-CoV-2 M^{pro}, showing a significantly low EC_{50} (0.075 μM) (Zhao et al., 2022). PF-00835231, initially designed for the M^{pro} of SARS-CoV, also inhibits SARS-CoV-2 with a low EC_{50} of 0.23 μM (Owen et al., 2021). GC376, a known cysteine protease covalent inhibitor targeting multiple viruses, exhibited antiviral activity against SARS-CoV-2 with an EC_{50} of 0.92 μM (Bai et al., 2021). Boceprevir, an approved serine protease inhibitor for treating Hepatitis C virus, demonstrated an EC_{50} of 15.57 μM against SARS-CoV-2 (Fu et al., 2020). Non-peptidomimetic inhibitors targeting the M^{pro} active site have also been identified, e.g., carmofur, ebselen, and MR6-31-2. Carmofur, an antineoplastic agent for colorectal cancer, exhibited an EC_{50} of 24.3 μM against SARS-CoV-2 (Jin et al., 2020b). Ebselen, an organoselenium molecule, forms a seleno-sulfide bond with thiol groups of cysteine on various proteins, leading to anti-inflammatory, antimicrobial, and neuroprotective effects (Azad and Tomar, 2014). Ebselen exhibits low cytotoxicity, and its safety profile has been assessed in multiple human clinical trials (Kil et al., 2017; Lynch and

96 Kil, 2009; Masaki et al., 2016). Ebselen and its derivative MR6-31-2 displayed promising
97 anti-SARS-CoV-2 activity with EC_{50} values of 4.67 μM and 1.78 μM, respectively
98 (Amporndanai et al., 2021). While these inhibitors mentioned above all covalently bind to
99 C145, they occupied different subsites (Figure S1) and formed different hydrogen bonds with
100 M^{pro} (Table 1), possibly correlating with their distinct inhibitory effect. Allosteric inhibitors
101 that non-covalently bind outside the active site of SARS-CoV-2 M^{pro} have been characterized
102 via X-ray screening (Günther et al., 2021). One such allosteric site is located in the cavity
103 between the catalytic and dimerization domains, to which AT7519 binds with an EC_{50} of
104 25.16 μM. Additionally, the C-terminal dimerization domain forms a hydrophobic pocket,
105 which accommodates the aromatic moiety of molecules, exemplified by pelitinib, which
106 exhibits an EC_{50} of 1.25 μM.
107
108 While these seven covalent-binding inhibitors showed marked differences in inhibitory
109 effects (EC_{50}, Table 1), structural alignment of M^{pro} showed that the active site pocket does
110 not undergo significant structural changes upon inhibitor binding (Figure S2). This suggests
111 that the divergent inhibitory effects are not attributable to major structural changes of M^{pro}
112 but likely arise from conformational changes of M^{pro} induced by inhibitor binding.
113 Hydrogen/deuterium exchange mass spectrometry (HDX-MS) is a powerful technique for
114 studying conformational dynamics of proteins and protein-drug complexes in solution by
115 monitoring deuterium exchange of the amide hydrogens of protein backbone (Huang et al.,
116 2019; James et al., 2021; Kish et al., 2023; Narang et al., 2020; Stofella et al., 2024).
117 Typically, amide hydrogens in more exposed and/or flexible regions exchange faster than
118 those at buried and/or rigid regions. Therefore, alterations in protein structures and dynamics
119 could be reflected by changes in HDX behaviors of amide hydrogens. Our group has
120 previously applied HDX-MS for studying the conformational dynamics of β-lactamases upon

121 binding with inhibitors, revealing promising allosteric sites as targets of drug development
122 (Huang et al., 2020a; 2021; Huang et al., 2025). Current HDX-MS investigations of M^{pro}
123 remain inadequate for a comprehensive elucidation of the inhibitory effects of these
124 inhibitors, as only the effect of PF-07321332 among these nine inhibitors on conformational
125 dynamics of M^{pro} has been presented by HDX-MS (Greasley et al., 2022; Yadav et al., 2022).
126 Furthermore, the dimerization process of M^{pro}, which is essential for its enzymatic function,
127 represents a promising yet relatively underexplored target in the field of drug discovery.
128 Intriguingly, the inhibitor PF-07321332, despite targeting the active site, has been reported to
129 promote M^{pro} dimerization by shifting the monomer-dimer equilibrium toward the dimeric
130 state (Higashi-Kuwata et al., 2023). This implies that the alterations in the dimerization
131 process may be another effect to reflect effective inhibitor binding, other than mainly via
132 direct blockade of the active site. To comprehensively advance our understanding of the
133 inhibitory mechanisms, it is essential to investigate the effects of these inhibitors on the
134 dimerization-related monomer-dimer equilibrium of M^{pro} and elucidate the conformational
135 dynamics alterations of M^{pro} induced by inhibitor binding.
136
137 In this study, we investigated the effects of three different types of inhibitors on the
138 monomer-dimer equilibrium and conformational dynamics changes of M^{pro} by integrating
139 isotope labeling, native MS, and HDX-MS. We characterized the significantly opposite
140 effects of peptidomimetic inhibitors and ebselen on monomer-dimer equilibrium and
141 conformational dynamics of M^{pro}. These findings underscore the importance of the dimer
142 interface regions as allosteric sites, offering valuable clues for the design of inhibitors
143 targeting M^{pro} dimerization.
144
145 **Results**

The monomer-dimer equilibrium modulation of M^{pro} induced by inhibitor binding

M^{pro} was characterized by native MS, and two well-resolved charge state distributions were readily identified. The results revealed an equilibrium in solution between monomer (9+ to 11+) and dimer species (14+ to 17+) of M^{pro}, with the dimer being the predominant form (Figure 1b), consistent with reported native MS results of M^{pro} (El-Baba et al., 2020). Deconvolution of the mass spectrum yielded a mass of 33,796 Da for the monomeric form (theoretical mass: 33,797 Da), and 67,840 Da for the dimeric form (theoretical mass: 67,594 Da). The 246 Da mass increment relative to the theoretical prediction of the dimer is likely due to the addition of solvent molecules and buffer ions, presumably at the dimer interfaces (Nettleton et al., 1998). Different inhibitors exert diverse effects on M^{pro} monomer-dimer equilibrium (Figures 1c,d and S3). The ratio of monomers decreased, and that of the dimer increased upon PF-07321332 binding, suggesting the monomer-dimer equilibrium of M^{pro} shifted toward the dimeric form (Figure 1c). This indicates that PF-07321332 not only binds to M^{pro} but also promotes its dimerization. The other three peptidomimetic inhibitors PF-00835231, GC376, and boceprevir also showed similar trends (Figure S3a-c). Taken together, these results suggest that when peptidomimetic inhibitors bind to the active site C145, they may induce the conformational change of M^{pro}. This perturbation may propagate from the active site to the dimer interface, ultimately promoting dimerization. Intriguingly, the allosteric inhibitor AT7519 also shifted the equilibrium toward the dimeric state (Figure S3f), aligning with previously published molecular dynamics (MD) simulation findings that AT7519 enhances both intra- and inter-domain coupling of M^{pro} (Zhang et al., 2024). Notably, the two non-peptidomimetic inhibitors, carmofur and MR6-31-2, did not significantly alter the monomer-dimer equilibrium (Figure S3d,e). Despite also covalently

binding to the active site C145, the impacts of carmofur and MR6-31-2 on the equilibrium differed from those of peptidomimetic inhibitors. The hydrogen bond interactions of residues E166 and S1are crucial for M^{pro} dimerization (Sacco *et al.*, 2020), and E166 can also form hydrogen bonds with all peptidomimetic inhibitors but not with non-peptidomimetic inhibitors (Table 1). The residue S1 from one monomer, the peptidomimetic inhibitor, and E166 from the other monomer form tight interactions, revealed by the enhanced hydrogen bond strength of residues S1 and E166 upon peptidomimetic binding compared to unbound M^{pro} (Figure S4). This bolstering of M^{pro} dimerization induced by peptidomimetic inhibitors may reflect the highly effective inhibitory effect of peptidomimetic inhibitors, as they firmly occupy the enzymatic active site pocket and competitively prevent the entry of SARS-CoV-2 immature polyproteins, thereby effectively preventing viral replication. It is worth noting that the promoted dimerization of the protease induced by inhibitor binding has been observed in the interactions between Human immunodeficiency Virus type 1 (HIV-1) protease and its inhibitors. In the presence of HIV-1 protease peptidomimetic inhibitors such as saquinavir and nelfinavir, levels of HIV-1 protease monomers decreased as they formed dimers bound to the inhibitors (Hayashi et al., 2014). This highlights the enzyme-specific nature of inhibition shared by both HIV-1 protease and SARS-CoV-2 M^{pro}.

Binding of ebselen (Figure 1d) and pelitinib (Figure S3g) to M^{pro} induced a significant shift toward the monomeric form, indicating dissociation of the dimer. Pelitinib was reported to engage in hydrophobic interactions with C-terminal amino acid residues at the dimer interface (Song et al., 2024). This binding may negatively impact the interactions among dimer interface residues and disrupt the dimer interface. The destabilization of M^{pro} was also revealed by a decrease in the melting temperature (T_m) of M^{pro} upon binding with ebselen (Ma et al., 2020). The fragment JGY and nanobody NB2B4 were reported to bind in the

195 dimer interface, destabilize the M^{pro} dimer, and showed inhibitory activity with an IC_{50} value
196 of 100 μM and 150 nM, respectively (El-Baba *et al.*, 2020; Sun et al., 2022). This suggests
197 that impairment of the M^{pro} dimer form may be associated with the inhibitory effect. While
198 ebselen was generally reported to bind to C145 for its inhibitory effect, our native MS results
199 revealed more than one ebselen binding to M^{pro} monomer and an increase in the amount of
200 M^{pro} monomers upon ebselen binding compared to unbound M^{pro} monomers (Figure 1d),
201 implying the ebselen-bound monomers are incapable of reassociating into dimers. We
202 speculate that ebselen binding may induce instability in the M^{pro} dimer interface, thereby
203 disrupting the dimer. Ebselen has not been previously reported to impair M^{pro} dimerization,
204 suggesting a potentially novel inhibitory mechanism of ebselen.
205

206 Subunit exchange dynamics of M^{pro} tuned by inhibitor binding

207 Subunit exchange is an effective process for analyzing the dissociation and association of
208 multimeric protein complexes (Yang et al., 2013), which can be monitored by native MS that
209 can retain and study intact proteins and protein complexes in their native states (Aquilina et
210 al., 2005; Sobott et al., 2002; Thangaraj et al., 2019; Uetrecht et al., 2010). As the monomer-
211 dimer equilibrium is reflected by the subunit exchange of the M^{pro} dimer, we employed
212 isotope labeling native MS to investigate the effect of inhibitors on subunit exchange
213 dynamics of M^{pro}. The strategy for subunit exchange is depicted in Figure 2a. As SARS-CoV-
214 2 M^{pro} ($^{12}C^{12}C$) is mixed with ^{13}C-labeled M^{pro} ($^{13}C^{13}C$), a new heterodimer ($^{12}C^{13}C$) occurs
215 due to dimer dissociation and monomer reassociation. These three dimers with different
216 masses can be monitored by native MS (Figures 2b and S5a,b). In contrast to free M^{pro}, the
217 heterodimer M^{pro} signal was undetected after PF-07321332 binding over the course of 30
218 minutes (Figure 2c). These findings imply that the PF-07321332 binding induces a structural
219 change that enhances the affinity of the dimer interface, thereby preventing dissociation.

220 Recent microcalorimetry experiments have provided additional evidence of strong
221 stabilization of M^{pro} by PF-07321332, as evidenced by a 10°C shift in T_m and a corresponding
222 increase of 10 kcal/mol in enthalpy (Paciaroni et al., 2023). In addition to PF-07321332,
223 peptidomimetic inhibitors PF-00835231, GC376, and boceprevir also significantly inhibited
224 subunit exchange, demonstrating their strong binding capacity with M^{pro}, although boceprevir
225 exhibited a relatively weaker effect (Figure 2d-f). These findings are consistent with our
226 monomer-dimer equilibrium results and suggest that peptidomimetic inhibitors can alter the
227 monomer-dimer equilibrium by preventing dimer dissociation. Intriguingly, ebselen also
228 inhibited subunit exchange of M^{pro} to a certain extent (Figure 2g). This effect may be
229 attributed to the binding of ebselen to the M^{pro} monomer, preventing its association into
230 dimers and thereby reducing the population of dimers. Carmofur and MR6-31-2 did not
231 change the subunit exchange (Figure S6b,c), consistent with our monomer-dimer equilibrium
232 results. For AT7519 and pelitinib binding, no significant effect on subunit exchange was
233 observed (Figure S6d,e), different from the monomer-dimer equilibrium findings, possibly
234 due to the reduced M^{pro}-to-inhibitor ratio (from 1:15 to 1:3). These results suggest that
235 AT7519 and pelitinib exhibit weak binding affinity for M^{pro}, and a higher inhibitor-to-M^{pro}
236 ratio will be required for subsequent HDX-MS study.
237

238 Conformational changes of M^{pro} upon inhibitor binding

239 HDX-MS was employed to provide conformational insights into the binding of inhibitors. By
240 optimizing the injected M^{pro} amount and quenching buffer, pepsin digestion of M^{pro} resulted
241 in 94.4% coverage of the entire sequence (Figure S7). Local HDX-MS of unbound M^{pro}
242 revealed relatively high deuterium uptake in the long loop regions, indicating the relatively
243 high flexibility (Figure 3a). This structural flexibility suggests that the long loop linker may
244 be flexible enough to effectively accommodate different groups of inhibitors. Conversely, the

245 N-terminal residues showed relatively low deuterium uptake, indicating that this region is
246 relatively more rigid (Figure 3a), possibly due to the hydrogen bonds associated with the N-
247 finger.
248
249 The effects of inhibitors on the conformational dynamics of M^{pro} were detected using global
250 and local HDX-MS. The global deuterium uptake of M^{pro} significantly decreased upon
251 binding with PF-07321332, indicating that the overall conformation of M^{pro} became more
252 rigid after the binding (Figure 3b). To obtain more detailed insights into the regional
253 conformational changes of M^{pro}, local HDX-MS was performed. Upon binding to PF-
254 07321332, significant changes in HDX were observed in certain active site regions (Figures
255 3c,d and S9a). Residues 35-47 and 135-150, encompassing the interacting residue H41 and
256 covalent binding site C145, exhibited significant decreases in deuterium uptakes, indicating
257 reduced flexibility, consistent with X-ray crystallography results that H41 and C145 formed
258 strong hydrogen bond and covalent bond interactions with the inhibitor molecule (Zhao *et al.*,
259 2022). Additionally, residues 160-177 in Domain II exhibited reduced deuterium uptake upon
260 PF-07321332 binding, which may be attributed to the hydrogen bond formation between
261 residue E166 and the inhibitor (Table 1). E166 is crucial for the correct orientation of the
262 active site pocket. Therefore, the reduced flexibility of this region could potentially influence
263 the formation of this subsite and consequently suppress the protein's activity. Interestingly, we
264 found that residues 104-111 and 116-125, which do not directly participate in the inhibitor
265 binding, also showed decreased deuterium uptake and thus reduced flexibility after the
266 binding, suggesting that these regions might modulate the binding of the inhibitor to the
267 active site by a short-range communication, enabling proper conformation. Furthermore,
268 residues 182-199, corresponding to the long loop linker connecting Domain II and Domain
269 III, demonstrated a highly significant decrease in deuterium uptake, implying that the

flexibility of this loop was reduced to a large extent upon binding to the inhibitor (Figure 3d). Q192 in this loop forms a hydrogen bond with the inhibitor molecule, which may be the primary interaction responsible for the loop's lower flexibility upon PF-07321332 binding. The residue D187 in this loop plays a crucial role in maintaining the charge of the catalytic H41 (Kneller et al., 2020). Thus, disturbing the plasticity of this loop upon inhibitor binding could impair the capacity of M^{pro} to accommodate various ligands and hydrolyze substrates, ultimately decreasing its activity. This observation aligns with previously reported M^{pro}-inhibitor complex simulations, which suggest that this loop exhibits reduced mobility upon binding to the inhibitor (Suárez and Díaz, 2020). Designing molecules that can interact with this large loop could be an attractive strategy for inhibition. In addition to the findings mentioned above, we newly discovered that the conformational dynamics of the N- and C-termini, which were not directly involved in inhibitor interactions, were significantly affected upon PF-07321332 binding. Residues 1-17 and 296-306 exhibited notable decreases in deuterium uptake upon the inhibitor binding, indicating that these regions became more rigid. The N- and C-termini are known to be dimer interface residues and crucial for the formation of the active dimeric form (Pekel et al., 2022; Zhao *et al.*, 2022). Thus, changes in their conformational dynamics could potentially impact the dimerization process. The conformational rigidity of the termini directly inhibits dimer dissociation, thereby accounting for the shift of the monomer-dimer equilibrium toward the dimeric state.

Comparative HDX-MS analysis revealed distinct conformational dynamics of M^{pro} induced by inhibitor binding. While GC376 and PF-00835231 induced similar HDX changes as those observed with PF-07321332 (Figures S8a,b, S9b,c and S11a,b), the magnitude of deuterium uptake alterations diverged significantly for boceprevir and carmofur compared to PF-07321332 (Figures S8c,d, S9d, S10a and S11c,d). Notably, boceprevir binding induced no

295 significant HDX changes in the N-terminal region, while carmofur binding left both the N-
296 and C-termini uptakes unchanged. These differential HDX profiles correspond with our
297 findings on subunit exchange: boceprevir obviously but incompletely disrupted subunit
298 exchange, whereas carmofur showed no significant effect. Additionally, the active site region
299 showed lower HDX reduction for boceprevir and carmofur relative to PF-07321332, with
300 similar trends observed in residues 104-111, 116-125, and the long loop linker, possibly due
301 to the different binding affinities of the inhibitors for M^{pro}. Ligands with higher affinity are
302 generally with slower off-rates, thereby maintaining their interactions with M^{pro} for longer
303 periods and inducing greater protection. Thus, the variations in deuterium uptake likely
304 reflect the differing abilities of inhibitors to stabilize M^{pro} dimerization state, which are
305 influenced by their binding strengths and relative on- and off-rates.
306
307 AT7519 and pelitinib are allosteric inhibitors that non-covalently bind outside of the active
308 site of M^{pro} (Günther *et al.*, 2021), indicating that M^{pro} may exhibit different conformational
309 dynamics when binding these inhibitors compared to those targeting the active site. Upon
310 binding with AT7519 or pelitinib, no significant differences in deuterium uptake of M^{pro} were
311 observed, even at a 50× molar excess of inhibitor relative to M^{pro} (Figure S10d,e). This may
312 indicate that AT7519 and pelitinib bind with M^{pro} with weak affinity, making it difficult to
313 detect any changes in deuterium uptake. A similar result was reported, showing that M^{pro}
314 exhibited no significant deuterium uptake difference when binding with pelitinib at a 50:1
315 molar ratio (pelitinib: M^{pro}) (Yadav *et al.*, 2022). The lack of observed HDX may stem from
316 experimental limitations in studying the weak interactions of binders using HDX-MS.
317
318 Remarkably, ebselen induced distinct conformational dynamics in M^{pro}, as global HDX-MS
319 analysis revealed higher structural flexibility upon binding of one and two ebselen molecules,

320 respectively (Figure 4a). This contrasts with the typical covalent inhibitors of M^{pro},
321 suggesting that ebselen may employ an entirely different inhibitory mechanism from others.
322 Ebselen binding resulted in an increased deuterium uptake across most regions of the M^{pro},
323 especially the N- and C-termini (Figures 4b,c and S10b). Our MD simulation also supports
324 this finding (Figure S13b-d), with an increased RMSF after binding. The increased flexibility
325 of these two terminal regions, combined with the native MS findings, indicates that the
326 conformational change of the N- and C-termini may relate to the monomer-dimer equilibrium
327 shift. The deprotection in the N-terminal region was also observed in MR6-31-2 binding,
328 implying a similar inhibitory mechanism to ebselen (Figures S8e, S10c and S11e).
329

330 **A new binding site of ebselen on M^{pro}**

331 Ebselen revealed multiple M^{pro} binding sites and exhibited distinct conformational dynamics
332 compared to other inhibitors, suggesting it may alter conformational dynamics of M^{pro} by
333 binding to cysteines outside the active site C145. To identify the binding sites of ebselen on
334 M^{pro}, liquid chromatography-tandem mass spectrometry (LC-MS/MS) was employed.
335 Incubation of M^{pro} with ebselen revealed ebselen-mediated cysteine modifications at C44 and
336 C300 (Figure S12). However, no adduct was observed on C145, aligning with observations
337 reported in previous structural analysis that a selenium-containing adduct on C145 was
338 identified arising from the hydrolysis reaction of ebselen (Amporndanai *et al.*, 2021).
339 However, the selenium-containing peptide with a single selenium atom bound to Cys145 was
340 also not identified in the software-based analysis. This selenium-modified peptide could
341 potentially cross-link with another selenium-containing peptide, which is typically
342 challenging to detect using search software. The crystal structure of the ebselen-M^{pro} complex
343 demonstrates that ebselen forms a covalent bond with C44 (PDB: 7BFB), aligning with our
344 MS findings. The C44A mutation has been shown to inhibit the activity of M^{pro}, highlighting

345 a significant role for C44 in M^{pro} activity (Iacobucci et al., 2025). These findings indicate that
346 ebselen may inactivate SARS-CoV-2 M^{pro} by covalently modifying C44, thereby impairing
347 the function of this essential viral protease. Additionally, reported MD simulations results
348 suggested that ebselen can bind at two probable sites: One at C145 within the catalytic cavity
349 via a Se-S bond, and the other at the dimerization region between Domain II and Domain III
350 (Menéndez et al., 2020). M^{pro} could be reversibly inhibited through the oxidation of C300
351 with glutathione, causing M^{pro} to form an inactive monomer (Davis et al., 2021). Tixocortol
352 has also been identified as an M^{pro} inhibitor that primarily targets C300, impairing M^{pro}
353 dimerization (Davis et al., 2024). Bismuth drug colloidal bismuth subcitrate (CBS) was
354 reported to bind to C300 of M^{pro} and result in dissociation of M^{pro} dimer and proteolytic
355 dysfunction (Tao et al., 2021). These results highlight an unexpected reactivity of additional
356 cysteine residues beyond the catalytic site C145, suggesting that a combination of inhibitory
357 mechanisms of inhibitors, rather than solely blocking the active site, is involved. Our HDX
358 results showed that residues 296-304 in the C-terminal region of M^{pro} were more flexible
359 upon ebselen binding (Figure 4c). This suggests that ebselen targeting C300 may induce
360 structural changes in the C-terminal helical segment, weakening key hydrogen bonds at the
361 dimer interface and ultimately inhibiting activity.
362
363 To gain deeper insight into the molecular mechanism of action of ebselen on M^{pro}, we
364 conducted an all-atom MD simulation to compare the structures and flexibility of M^{pro} before
365 and after ebselen binding at C300. We performed 1000 ns of MD simulations in triplicate
366 (Figure S13) to investigate the interactions of key amino acids at the dimeric interface
367 (residues S1 and E166, and R4 and E290), which are essential for maintaining the dimeric
368 form of M^{pro}. For the ebselen-modified M^{pro}, the Cα distance between R4 of the N-finger of
369 one monomer and the E290 of Domain III of the other monomer changed from 7.5 Å to 10.5

Å after ebselen binding. Additionally, the Cα atoms distance between S1 on the N-finger of each monomer and E166 on Domain II of the other monomer increased from 13.0 Å to 15.5 Å (Figure 4d). These observations suggested that covalent modification of ebselen at C300 may reduce the intensity of M^{pro} dimer hydrogen bond, thereby inducing a steric blocking of dimer formation. Given its unique positioning at the dimeric surface, mutation or modification of the conserved C300 may impair M^{pro} dimerization and further cause the active enzyme to form an inactive monomer, offering new avenues for designing novel agents to combat SARS-CoV-2.

Discussion

This study investigates SARS-CoV-2 M^{pro} as a critical antiviral drug target and reveals the distinct effects of peptidomimetic inhibitors and ebselen on SARS-CoV-2 M^{pro} dimerization and conformational change. Peptidomimetic inhibitors stabilize the M^{pro} dimer form by rigidifying the N- and C-termini, thereby suppressing subunit exchange of M^{pro} dimer and shifting the monomer-dimer equilibrium of M^{pro} toward the dimeric state. The interaction of M^{pro} and peptidomimetic may firmly lock dimeric M^{pro} in a compact M^{pro}-inhibitor complex state, which is inactive for M^{pro} proteolytic activity by effectively competing with substrates for binding and inhibiting substrate cleavage. In contrast, ebselen covalently binds to C300, a critical residue at the dimer interface, thereby inducing conformational flexibility in the C-terminal region and shifting the monomer-dimer equilibrium of M^{pro} toward the inactive monomeric state, representing a novel allosteric inhibition mechanism of ebselen. The conserved nature of the M^{pro} dimer interface across coronavirus species suggests that targeting this region could lead to the development of broad-spectrum antivirals. Especially, the identification of C300 as a druggable allosteric hotspot offers an alternative strategy to combat drug resistance arising from active site mutations.

395 More generally, the therapeutic potential of inhibitors can be readily assessed by the
396 relatively straightforward dual MS approaches, which involve probing the monomer-dimer
397 equilibrium and the conformational dynamics of M^{pro} upon inhibitor binding. These
398 measurements elucidate the mechanism of action of these inhibitors, either through binding to
399 the active site or by influencing the dimer interface, thereby disrupting or favoring
400 dimerization. This work establishes a paradigm for exploring allosteric modulation in SARS-
401 CoV-2 M^{pro} and provides new ways for assessing the efficacy of novel antiviral drug
402 candidates against M^{pro} in SARS-CoV-2 and emerging coronaviruses.

403 **Methods**

404 **Materials**

405 PF-07321332, PF-00835231, boceprevir, carmofur, ebselen, AT7519, and pelitinib were
406 purchased from MedChemExpress (Princeton, NJ, USA). GC376 was purchased from
407 Selleckchem (Houston, USA). MR6-31-2 was purchased from Sigma-Aldrich (St. Louis,
408 USA). All inhibitors were dissolved in 100% dimethyl sulfoxide (DMSO) to achieve the
409 desired concentrations, while ensuring that the DMSO concentration remained below 5% in
410 all inhibitor-protein mixtures. Tag-free authentic SARS-CoV-2 M^{pro} (Cat# SAE0172) was
411 from Sigma-Aldrich (St. Louis, USA). Tag-free SARS-CoV-2 M^{pro} and ^{13}C-labeled SARS-
412 CoV-2 M^{pro} were produced from Beijing Anbiqi Biotechnology Co., Ltd (Beijing, China).
413 Deuterium oxide was purchased from Cambridge Isotope Laboratories (Tewksbury, USA).
414 Formic acid (MS grade) was purchased from Sigma-Aldrich (St. Louis, USA), and
415 acetonitrile (LC-MS grade) was acquired from Anaqua (DE, USA). Ultra-centrifugal filters
416 with 10 kDa molecular weight cut-off were purchased from Millipore (Burlington, USA).

417

418 **Native mass spectrometry**

419 Native MS analysis was performed using nano-electrospray ionization (nano-ESI) on a

420 Waters Synapt G2-Si. The protein samples were buffer-exchanged into 200 mM ammonium
421 acetate utilizing 10 kDa cut-off ultra-centrifugal filters. M^{pro} was incubated with inhibitors for
422 30 minutes at room temperature before ESI. Typically, 3 μL sample was loaded into
423 homemade gold-coated glass nano-ESI emitters for analysis. Nano-ESI capillaries were
424 fabricated in-house from borosilicate glass tubes with outer and inner diameters of 1 mm and
425 0.75 mm, respectively (Sutter Instruments, Hercules, CA). Preparation involved using a P-
426 2000 laser-based micropipette puller (Sutter Instruments, Hercules, CA), followed by gold
427 coating with a 150R S Plus sputter coater (Electron Microscopy Sciences, PA, USA). Typical
428 settings in positive ion mode included: capillary voltage at 1.5 kV, sampling cone at 30 V,
429 source offset at 30 V, source temperatures at 30°C, gas flows cone gas at 30 L/h, trap collision
430 energy (CE) at 50 V, transfer CE at 50 V, and gas control trap at 6 mL/min. All spectra were
431 internally calibrated using a cesium iodide solution, with spectral acquisition over a range of
432 1000-7000 *m/z*. Data analysis was performed using MassLynx v4.2 software, with no
433 background subtraction and minimal smoothing applied.
434

435 **Subunit exchange**

436 Label-free SARS-CoV-2 M^{pro} was mixed with ^{13}C-labeled SARS-CoV-2 M^{pro} for varying
437 time intervals, and the extent of subunit exchange was monitored using native MS. To
438 investigate the effect of inhibitors on the M^{pro} subunit exchange, M^{pro} was incubated with
439 inhibitors at a ratio of 1:3 (5 μM:15 μM) for 30 minutes at room temperature before mixing
440 with an equal volume of 5 μM ^{13}C-labeled SARS-CoV-2 M^{pro}. The extent of the subunit
441 exchange was monitored at 5 min and 30 min, respectively.
442

443 **Global and local Hydrogen/deuterium exchange mass spectrometry (HDX-**
444 **MS)**

445 HDX-MS experiments were performed on a Waters Synapt G2-Si, following protocols
446 similar to those described in our previous studies (Huang et al., 2020b). M^{pro} was incubated
447 with covalent inhibitors at a ratio of 1:3 or allosteric inhibitors at a ratio of 1:50 for 30
448 minutes at room temperature before HDX experiments. 10 pmol of samples (for global HDX-
449 MS) or 50 pmol of samples (for local HDX-MS) were labeled with 9× volume deuterated
450 PBS buffer at various time points. Each sample was then quenched by diluting 1:1 into a
451 quenching buffer (3.2% formic acid in ddH_2O). For global HDX-MS analysis, the quenched
452 mixtures were loaded onto a Waters ACQUITY UPLC Protein BEH C4 VanGuard Pre-
453 column (300 Å, 1.7 µm, 2.1 mm × 50 mm) and washed for 3 minutes. Subsequently, samples
454 were separated on a Waters ACQUITY UPLC Protein BEH C4 Column (300 Å, 1.7 µm, 2.1
455 mm × 100 mm), using a 10-minute linear gradient from 20% to 80% solvent B (0.1% FA,
456 100% acetonitrile). For local HDX-MS analysis, the quenched mixture underwent online
457 pepsin digestion at 20°C using a Water BEH Enzymate Pepsin Column (300 Å, 5 µm, 2.1
458 mm × 30 mm). The resulting peptides were trapped on a Waters ACQUITY UPLC BEH C18
459 VanGuard Pre-column (130 Å, 1.7 µm, 2.1 mm × 5 mm) and desalted for 3 minutes.
460 Subsequently, the peptides were separated on a Waters ACQUITY UPLC BEH C18 Column
461 (130 Å, 1.7 µm, 1 mm × 100 mm), using a 12-minute linear gradient from 5% to 95% solvent
462 B. For peptide identification, non-deuterated samples were analyzed using the same LC
463 method. The reference mass of each peptide was generated using the same HDX-MS
464 procedure, in which all D_2O was replaced with ddH_2O. A clean blank was injected between
465 each analytical run to eliminate any carryover.
466

467 **HDX-MS Data analysis**

468 Data for each time point were collected in triplicate. The results are presented as mean values
469 ± standard deviation (SD), where error bars indicate the standard deviation for each time

point. For global HDX-MS data, the acquired spectra were deconvolved using MassLynx 4.2 to determine the deuterated protein mass at various time points. Deuterium uptake was calculated by subtracting the mass of the non-deuterated protein from that of the deuterated protein using Microsoft Excel. Pairwise comparisons of deuterium uptake between different states were statistically analyzed using a two-tailed Student's *t*-test. Significance levels are denoted based on the *t*-test results as follows: *ns* for $P > 0.05$ (not significant), * for $P < 0.05$, ** for $P < 0.01$, and *** for $P < 0.001$. For local HDX-MS data, the MS^E spectra were processed with ProteinLynx Global Server 3.0.2 (PLGS, Waters, UK) for peptide identification. The resulting peptides were further filtered using DynamX 3.0 (Waters, UK) with the following parameters: a minimum intensity of 5000, a minimum product ions per amino acid of 0.15, a maximum ppm mass error on the precursor ion of 10, and a minimum score of 6.5. HDX measurements were performed in triplicate, and the relative deuterium uptake for peptides was based on the average of these replicates. Sequence coverage, redundancy, number of generated peptides, repeatability, and significant difference in HDX were calculated automatically using Deuteros software (Lau et al., 2021). A significance threshold was established to assess differences in HDX between states compared in each dataset, corresponding to a 99% confidence interval (CI) calculated from triplicate measures for each comparative HDX dataset. A hybrid significance test with a 99.0% confidence interval was employed for all datasets presented in Woods plots using Deuteros 2.0. The line plots and bar plots were generated using GraphPad Prism 8. For visualization, relative fractional deuterium uptake and relative fractional deuterium uptake differences were mapped onto the M^{pro} crystal structure (PDB entry 7ALI) using PyMOL 3.1. To facilitate access to the HDX data obtained in this study, the HDX Summary Table is included in the Supporting Information, as recommended by the community (Masson et al., 2019).

495 **Identification of binding sites of ebselen on M^{pro}**

496 M^{pro} was incubated with ebselen at a molar ratio of 2:1 and 1:3 at room temperature for 30
497 minutes, respectively. The mixture was then denatured and digested with trypsin. The
498 resulting peptides were desalted and dried. Samples were analyzed on a Bruker timsTOF Pro
499 2 Mass Spectrometer (Bruker, Bremen, Germany) coupled with a Thermo Fisher Scientific
500 UltiMate 3000 RSLCnano (Waltham, USA). Dried peptide samples were dissolved in 0.1%
501 formic acid in water and loaded onto an Acclaim™ PepMap™ 100 C18 trap column (5 mm ×
502 1 mm; particle size, 5 μm; pore size, 100 Å; Thermo Fisher Scientific, Waltham, USA).
503 Peptides were then separated on an Aurora™ ULTIMATE C18 analytical column (25 cm ×
504 75 μm; particle size, 1.7 μm; pore size, 120 Å; IonOpticks, Fitzroy, Australia) using a gradient
505 of 5–35% mobile phase B (acetonitrile and 0.1% formic acid) at a flow rate of 300 nL/min
506 over 45 minutes. MS and MS/MS spectra were acquired with a mass scan range of 100-1700
507 *m/z* and an ion mobility scan range of 0.6-1.6 V•s/cm^2. The dual TIMS setup enabled
508 operation at a 100% duty cycle, with ramp and accumulation times set at 100 ms. MS/MS
509 spectra were acquired using DDA-PASEF (Data-dependent acquisition-Parallel
510 Accumulation-Serial Fragmentation) mode. Database searches were performed using PEAKS
511 Studio 12.0, employing a database downloaded from the NCBI Reference Sequence
512 (YP_009725301.1) for SARS-CoV-2 M^{pro}. The protein identification search was conducted
513 with the following parameters: variable modifications included methionine oxidation
514 (+15.995 Da), acetylation (+42.011 Da) at the N-terminus, and cysteine ebselen modification
515 (+275 Da); trypsin digestion was allowed with up to two missed cleavages. Other parameters
516 were set to the software defaults.

517

518 **Molecular dynamics (MD) simulation**

519 The initial conformation of the SARS-CoV-2 M^{pro} model was obtained from the PDB

520 database (PDB ID: 7ALI). We also constructed a model of ebselen-bound M^{pro} (to C300, both
521 chains). We referred to another crystal structure (PDB ID: 7BFB). In 7BFB, an ebselen ligand
522 was found near C300 of chain B (not in chain A), but most of the ligand is not defined (has
523 no electron density) except for the selenium. The geometry of the ebselen-modified C300 was
524 poor (S-Se bond too long). Therefore, we built the ebselen-modified M^{pro} model such that it
525 is covalently bound to a suitable rotamer of the C300 residue of both protomers, while
526 avoiding steric clash with nearby protein atoms. The covalent bond between ebselen and
527 C300 is patched with PyMOL and optimized with Sculpting. MD simulations were set up
528 using the Amber 22 software package with GPU-accelerated PMEMD (Particle Mesh Ewald
529 Molecular Dynamics) (Case et al., 2023). The ff14SB force field was applied to generate
530 parameters for the protein (Maier et al., 2015). Because the ligands contain selenium atoms,
531 which are not included in the General Amber Force Field (GAFF), the restrained electrostatic
532 potential (RESP) protocol with HF/6-31G* was employed to calculate the atomic charges for
533 the ebselen. Force field parameters for ebselen and modified cysteine were determined using
534 the Antechamber module of Amber 22. Na(I) counter ions were included to neutralize the
535 charges. The protein structure was solvated in a TIP3P periodic box with a minimum distance
536 of 10 Å from the box edge. The first minimization involves 6000 steepest descent steps with
537 a constant volume periodic boundary, and a second minimization (6000 steps) with no
538 constraints of conjugate gradient energy minimization. Next, the temperature gradually
539 increased from 0 to 298 K over 20 ps using a Langevin thermostat. Density equilibration and
540 production runs were carried out using a constant pressure ensemble (NPT). The SHAKE was
541 applied to constrain the bond length of hydrogen atoms at equilibrium and production stages.
542 Long-range electrostatic interactions were treated using the Particle Mesh Ewald (PME)
543 method, with a nonbonded interaction cutoff of 8 Å. For both the SARS-CoV-2 M^{pro} and
544 SARS-CoV-2 M^{pro}-ebselen systems, three independent trajectories were performed with

random seeds. Simulations were performed at the same temperature with HDX-MS (298 K) for 1000 ns, with a step size of 200 ps, resulting in a total of 5000 snapshots. Root mean square deviation (RMSD), root mean square fluctuation (RMSF), and distances between specified atoms in each MD snapshot were calculated using the CPPTRAJ module in AMBER 22.

Acknowledgments

We thank Dr. Yu Wai Chen, Dr. Tsz Fung Wong and other members of the Yao group for their assistances and helpful discussion. We thank Dr. Sirius Pui-Kam Tse, Dr. Pui-Kin So, and Dr. Chi-Hang Chow for their assistance with the project. This work was supported by the National Key Research and Development Program of China (Grant No. 2024YFF0725800), and Hong Kong Research Grants Council (Grant Nos. 15304022, 15308923, R5013-19, C5026-24G, C5031-14E, C4014-23G, and CRS_CUHK405/23). We thank the University Research Facility in Life Sciences and the University Research Facility in Chemical and Environmental Analysis at The Hong Kong Polytechnic University for the technical and instrumental support.

Additional information

Competing interests

The authors declare that they have no known competing financial interests or personal relationships that could have appeared to influence the work reported in this paper.

Author contributions

Chengxi Liu: Writing – original draft, Methodology, Investigation. Qinyu Jia: Writing – review & editing, Methodology. Chang Zhao: Writing – review & editing, Investigation.

570 Zhongping Yao: Writing – review & editing, Supervision, Conceptualization, Funding
571 acquisition.
572

573 ## Additional files

574 **Supplementary files**

575 Supporting information includes structural alignments, mass spectra of native MS and HDX-
576 MS, deuterium uptake lines and wood plots, LC-MS/MS results, and MD simulation
577 (Supplementary Figures S1-S13). Summaries of HDX experimental details (Table S1).
578

579 **Data and code availability**

580 All data supporting this study are available within the main article and supplemental
581 information. This study did not generate any datasets or original code.

582 ## References

583 Amporndanai, K, Meng, X, Shang, W, Jin, Z, Rogers, M, Zhao, Y, Rao, Z, Liu, Z-J, Yang, H,
584 and Zhang, L. 2021. Inhibition mechanism of SARS-CoV-2 main protease by ebselen and its
585 derivatives. *Nature communications* **12**, 3061. doi: 10.1038/s41467-021-23313-7.

586 Aquilina, JA, Benesch, JL, Ding, LL, Yaron, O, Horwitz, J, and Robinson, CV. 2005. Subunit
587 exchange of polydisperse proteins: mass spectrometry reveals consequences of alphaA-
588 crystallin truncation. *J Biol Chem* **280**, 14485–91. doi: 10.1074/jbc.M500135200.

589 Azad, GK, and Tomar, RS. 2014. Ebselen, a promising antioxidant drug: mechanisms of
590 action and targets of biological pathways. *Mol Biol Rep* **41**, 4865–79. doi: 10.1007/s11033-
591 014-3417-x.

592 Bai, Y, Ye, F, Feng, Y, Liao, H, Song, H, Qi, J, Gao, GF, Tan, W, Fu, L, and Shi, Y. 2021.
593 Structural basis for the inhibition of the SARS-CoV-2 main protease by the anti-HCV drug
594 narlaprevir. *Signal transduction and targeted therapy* **6**, 51. doi: 10.1038/s41392-021-00468-
595 9.

596 Case, DA, Aktulga, HM, Belfon, K, Cerutti, DS, Cisneros, GA, Cruzeiro, VWD, Forouzesh,
597 N, Giese, TJ, Götz, AW, Gohlke, H, Izadi, S, Kasavajhala, K, Kaymak, MC, King, E,
598 Kurtzman, T, Lee, TS, Li, P, Liu, J, Luchko, T, Luo, R, Manathunga, M, Machado, MR,
599 Nguyen, HM, O'Hearn, KA, Onufriev, AV, Pan, F, Pantano, S, Qi, R, Rahnamoun, A, Risheh,
600 A, Schott-Verdugo, S, Shajan, A, Swails, J, Wang, J, Wei, H, Wu, X, Wu, Y, Zhang, S, Zhao,
601 S, Zhu, Q, Cheatham, TE, 3rd, Roe, DR, Roitberg, A, Simmerling, C, York, DM, Nagan, MC,

and Merz, KM, Jr. 2023. AmberTools. *J Chem Inf Model* **63**, 6183–91. doi: 10.1021/acs.jcim.3c01153.

Chou, C-Y, Chang, H-C, Hsu, W-C, Lin, T-Z, Lin, C-H, and Chang, G-G. 2004. Quaternary structure of the severe acute respiratory syndrome (SARS) coronavirus main protease. *Biochemistry* **43**, 14958–70. doi: 10.1021/bi0490237.

Davis, DA, Bulut, H, Shrestha, P, Yaparla, A, Jaeger, HK, Hattori, S-i, Wingfield, PT, Mieyal, JJ, Mitsuya, H, and Yarchoan, R. 2021. Regulation of the dimerization and activity of SARS-CoV-2 main protease through reversible glutathionylation of cysteine 300. *MBio* **12**, 10.1128/mbio. 02094–21. doi: 10.1128/mBio.02094-21.

Davis, DA, Nair, A, Astter, Y, Treco, E, Peyser, B, Gussio, R, Nguyen, T, Eaton, B, Postnikova, E, and Murphy, M. 2024. Discovery of a nasal spray steroid, tixocortol, as an inhibitor of SARS-CoV-2 main protease and viral replication. *RSC Medicinal Chemistry* **15**, 4193–205. doi: 10.1039/d4md00454j.

Deshmukh, MG, Ippolito, JA, Zhang, C-H, Stone, EA, Reilly, RA, Miller, SJ, Jorgensen, WL, and Anderson, KS. 2021. Structure-guided design of a perampanel-derived pharmacophore targeting the SARS-CoV-2 main protease. *Structure* **29**, 823–33. e5. doi: 10.1016/j.str.2021.06.002.

El-Baba, TJ, Lutomski, CA, Kantsadi, AL, Malla, TR, John, T, Mikhailov, V, Bolla, JR, Schofield, CJ, Zitzmann, N, Vakonakis, I, and Robinson, CV. 2020. Allosteric inhibition of the SARS-CoV-2 Main protease: insights from mass spectrometry based assays. *Angewandte Chemie International Edition* **59**, 23544–48. doi: 10.1002/anie.202010316.

Fu, L, Ye, F, Feng, Y, Yu, F, Wang, Q, Wu, Y, Zhao, C, Sun, H, Huang, B, and Niu, P. 2020. Both Boceprevir and GC376 efficaciously inhibit SARS-CoV-2 by targeting its main protease. *Nature communications* **11**, 4417. doi: 10.1038/s41467-020-18233-x.

Gao, Y, Kaub, J, Santoni, G, Pearce, N, and Thorn, A. 2023. Structural biology of SARS-CoV-1/SARS-CoV-2 main protease. *Crystallography Reviews* **29**, 76–101. doi: 10.1080/0889311X.2023.2222275.

Goyal, B, and Goyal, D. 2020. Targeting the dimerization of the main protease of coronaviruses: a potential broad-spectrum therapeutic strategy. *ACS combinatorial science* **22**, 297–305. doi: 10.1021/acscombsci.0c00058.

Greasley, SE, Noell, S, Plotnikova, O, Ferre, R, Liu, W, Bolanos, B, Fennell, K, Nicki, J, Craig, T, and Zhu, Y. 2022. Structural basis for the in vitro efficacy of nirmatrelvir against SARS-CoV-2 variants. *Journal of Biological Chemistry* **298**. doi: 10.1016/j.jbc.2022.101972.

Günther, S, Reinke, PY, Fernández-García, Y, Lieske, J, Lane, TJ, Ginn, HM, Koua, FH, Ehrt, C, Ewert, W, and Oberthuer, D. 2021. X-ray screening identifies active site and

allosteric inhibitors of SARS-CoV-2 main protease. *Science* **372**, 642–46. doi: 10.1126/science.abf7945.

Hayashi, H, Takamune, N, Nirasawa, T, Aoki, M, Morishita, Y, Das, D, Koh, Y, Ghosh, AK, Misumi, S, and Mitsuya, H. 2014. Dimerization of HIV-1 protease occurs through two steps relating to the mechanism of protease dimerization inhibition by darunavir. *Proceedings of the National Academy of Sciences* **111**, 12234–39. doi: 10.1073/pnas.1400027111.

Higashi-Kuwata, N, Tsuji, K, Hayashi, H, Bulut, H, Kiso, M, Imai, M, Ogata-Aoki, H, Ishii, T, Kobayakawa, T, and Nakano, K. 2023. Identification of SARS-CoV-2 Mpro inhibitors containing P1'4-fluorobenzothiazole moiety highly active against SARS-CoV-2. *Nature Communications* **14**, 1076. doi: 10.1038/s41467-023-36729-0.

Hoffman, RL, Kania, RS, Brothers, MA, Davies, JF, Ferre, RA, Gajiwala, KS, He, M, Hogan, RJ, Kozminski, K, and Li, LY. 2020. Discovery of ketone-based covalent inhibitors of coronavirus 3CL proteases for the potential therapeutic treatment of COVID-19. *Journal of medicinal chemistry* **63**, 12725–47. doi: 10.1021/acs.jmedchem.0c01063.

Huang, L, So, P-K, Chen, YW, Leung, Y-C, and Yao, Z-P. 2020a. Conformational dynamics of the helix 10 region as an allosteric site in class A β-lactamase inhibitory binding. *Journal of the American Chemical Society* **142**, 13756–67. doi: 10.1021/jacs.0c04088.

Huang, L, So, P-K, Chen, YW, Leung, Y-C, and Yao, Z-P. 2021. Interdomain flexibility and interfacial integrity of β-lactamase inhibitory protein (BLIP) modulate its binding to class A β-lactamases. *Journal of Biological Chemistry* **297**. doi: 10.1016/j.jbc.2021.100980.

Huang, L, So, PK, Chen, YW, Leung, YC, and Yao, ZP. 2020b. Conformational Dynamics of the Helix 10 Region as an Allosteric Site in Class A β-Lactamase Inhibitory Binding. *J Am Chem Soc* **142**, 13756–67. doi: 10.1021/jacs.0c04088.

Huang, L, So, PK, and Yao, ZP. 2019. Protein dynamics revealed by hydrogen/deuterium exchange mass spectrometry: Correlation between experiments and simulation. *Rapid Communications in Mass Spectrometry* **33**, 83–89. doi: 10.1002/rcm.8307.

Huang, L, Wong, T-F, Cheng, Q, So, P-K, Liu, M, Li, X, Chen, S, and Yao, Z-P. 2025. Inhibitor-Dependent Tolerance of New Delhi Metallo-β-Lactamase Driven by Single Mutation-Induced Conformational Changes. *Journal of the American Chemical Society* **147**, 26389−401. doi: 10.1021/jacs.5c05669.

Iacobucci, I, Cipollone, I, Cozzolino, F, Iaconis, D, Talarico, C, Coppola, G, Morasso, S, Costanzi, E, Malune, P, and Storici, P. 2025. Cys44 of SARS-CoV-2 3CLpro affects its catalytic activity. *International Journal of Biological Macromolecules* **295**, 139590. doi: 10.1016/j.ijbiomac.2025.139590.

James, EI, Murphree, TA, Vorauer, C, Engen, JR, and Guttman, M. 2021. Advances in hydrogen/deuterium exchange mass spectrometry and the pursuit of challenging biological

systems. *Chemical reviews* **122**, 7562–623. doi: 10.1021/acs.chemrev.1c00279.

Jin, Z, Du, X, Xu, Y, Deng, Y, Liu, M, Zhao, Y, Zhang, B, Li, X, Zhang, L, and Peng, C. 2020a. Structure of Mpro from SARS-CoV-2 and discovery of its inhibitors. *Nature* **582**, 289–93. doi: 10.1038/s41586-020-2223-y.

Jin, Z, Zhao, Y, Sun, Y, Zhang, B, Wang, H, Wu, Y, Zhu, Y, Zhu, C, Hu, T, and Du, X. 2020b. Structural basis for the inhibition of SARS-CoV-2 main protease by antineoplastic drug carmofur. *Nature structural & molecular biology* **27**, 529–32. doi: 10.1038/s41594-020-0440-6.

Jochmans, D, Liu, C, Donckers, K, Stoycheva, A, Boland, S, Stevens, SK, De Vita, C, Vanmechelen, B, Maes, P, Trüeb, B, Ebert, N, Thiel, V, De Jonghe, S, Vangeel, L, Bardiot, D, Jekle, A, Blatt, LM, Beigelman, L, Symons, JA, Raboisson, P, Chaltin, P, Marchand, A, Neyts, J, Deval, J, and Vandyck, K. 2023. The Substitutions L50F, E166A, and L167F in SARS-CoV-2 3CLpro Are Selected by a Protease Inhibitor In Vitro and Confer Resistance To Nirmatrelvir. *mBio* **14**, e0281522. doi: 10.1128/mbio.02815-22.

Kil, J, Lobarinas, E, Spankovich, C, Griffiths, SK, Antonelli, PJ, Lynch, ED, and Le Prell, CG. 2017. Safety and efficacy of ebselen for the prevention of noise-induced hearing loss: a randomised, double-blind, placebo-controlled, phase 2 trial. *The lancet* **390**, 969–79. doi: 10.1016/S0140-6736(17)31791-9.

Kish, M, Ivory, DP, and Phillips, JJ. 2023. Transient Structural Dynamics of Glycogen Phosphorylase from Nonequilibrium Hydrogen/Deuterium-Exchange Mass Spectrometry. *Journal of the American Chemical Society* **146**, 298–307. doi: 10.1021/jacs.3c08934.

Kneller, DW, Phillips, G, O'Neill, HM, Tan, K, Joachimiak, A, Coates, L, and Kovalevsky, A. 2020. Room-temperature X-ray crystallography reveals the oxidation and reactivity of cysteine residues in SARS-CoV-2 3CL Mpro: insights into enzyme mechanism and drug design. *IUCrJ* **7**, 1028–35. doi: 10.1107/S2052252520012634.

Lau, AM, Claesen, J, Hansen, K, and Politis, A. 2021. Deuteros 2.0: peptide-level significance testing of data from hydrogen deuterium exchange mass spectrometry. *Bioinformatics* **37**, 270–72. doi: 10.1093/bioinformatics/btaa677.

Lynch, E, and Kil, J (2009). Development of ebselen, a glutathione peroxidase mimic, for the prevention and treatment of noise-induced hearing loss. In 01. (© Thieme Medical Publishers), pp. 047–55. doi: 10.1016/j.heares.2006.08.006.

Ma, C, Hu, Y, Townsend, JA, Lagarias, PI, Marty, MT, Kolocouris, A, and Wang, J. 2020. Ebselen, disulfiram, carmofur, PX-12, tideglusib, and shikonin are nonspecific promiscuous SARS-CoV-2 main protease inhibitors. *ACS pharmacology & translational science* **3**, 1265–77. doi: 10.1101/2020.09.15.299164.

Maier, JA, Martinez, C, Kasavajhala, K, Wickstrom, L, Hauser, KE, and Simmerling, C.

2015. ff14SB: Improving the Accuracy of Protein Side Chain and Backbone Parameters from ff99SB. *J Chem Theory Comput* **11**, 3696–713. doi: 10.1021/acs.jctc.5b00255.

Masaki, C, Sharpley, AL, Cooper, CM, Godlewska, BR, Singh, N, Vasudevan, SR, Harmer, CJ, Churchill, GC, Sharp, T, and Rogers, RD. 2016. Effects of the potential lithium-mimetic, ebselen, on impulsivity and emotional processing. *Psychopharmacology* **233**, 2655–61. doi: 10.1007/s00213-016-4319-5.

Masson, GR, Burke, JE, Ahn, NG, Anand, GS, Borchers, C, Brier, S, Bou-Assaf, GM, Engen, JR, Englander, SW, Faber, J, Garlish, R, Griffin, PR, Gross, ML, Guttman, M, Hamuro, Y, Heck, AJR, Houde, D, Iacob, RE, Jørgensen, TJD, Kaltashov, IA, Klinman, JP, Konermann, L, Man, P, Mayne, L, Pascal, BD, Reichmann, D, Skehel, M, Snijder, J, Strutzenberg, TS, Underbakke, ES, Wagner, C, Wales, TE, Walters, BT, Weis, DD, Wilson, DJ, Wintrode, PL, Zhang, Z, Zheng, J, Schriemer, DC, and Rand, KD. 2019. Recommendations for performing, interpreting and reporting hydrogen deuterium exchange mass spectrometry (HDX-MS) experiments. *Nat Methods* **16**, 595–602. doi: 10.1038/s41592-019-0459-y.

Menéndez, CA, Byléhn, F, Perez-Lemus, GR, Alvarado, W, and de Pablo, JJ. 2020. Molecular characterization of ebselen binding activity to SARS-CoV-2 main protease. *Science Advances* **6**, eabd0345. doi: 10.1126/sciadv.abd0345.

Narang, D, Lento, C, and J. Wilson, D. 2020. HDX-MS: an analytical tool to capture protein motion in action. *Biomedicines* **8**, 224. doi: 10.3390/biomedicines8070224.

Nettleton, EJ, Sunde, M, Lai, Z, Kelly, JW, Dobson, CM, and Robinson, CV. 1998. Protein subunit interactions and structural integrity of amyloidogenic transthyretins: evidence from electrospray mass spectrometry. *J Mol Biol* **281**, 553–64. doi: 10.1006/jmbi.1998.1937.

Owen, DR, Allerton, CM, Anderson, AS, Aschenbrenner, L, Avery, M, Berritt, S, Boras, B, Cardin, RD, Carlo, A, and Coffman, KJ. 2021. An oral SARS-CoV-2 Mpro inhibitor clinical candidate for the treatment of COVID-19. *Science* **374**, 1586–93. doi: 10.1126/science.abl4784.

Paciaroni, A, Libera, V, Ripanti, F, Orecchini, A, Petrillo, C, Francisci, D, Schiaroli, E, Sabbatini, S, Gidari, A, and Bianconi, E. 2023. Stabilization of the dimeric state of SARS-CoV-2 main protease by GC376 and nirmatrelvir. *International Journal of Molecular Sciences* **24**, 6062. doi: 10.3390/ijms24076062.

Pekel, H, Ilter, M, and Sensoy, O. 2022. Inhibition of SARS-CoV-2 main protease: a repurposing study that targets the dimer interface of the protein. *Journal of Biomolecular Structure and Dynamics* **40**, 7167–82. doi: 10.1080/07391102.2021.1910571.

Sacco, MD, Ma, C, Lagarias, P, Gao, A, Townsend, JA, Meng, X, Dube, P, Zhang, X, Hu, Y, and Kitamura, N. 2020. Structure and inhibition of the SARS-CoV-2 main protease reveal strategy for developing dual inhibitors against Mpro and cathepsin L. *Science Advances* **6**, eabe0751. doi: 10.1126/sciadv.abe0751.

Sobott, F, Benesch, JL, Vierling, E, and Robinson, CV. 2002. Subunit exchange of multimeric

protein complexes. Real-time monitoring of subunit exchange between small heat shock proteins by using electrospray mass spectrometry. *J Biol Chem* **277**, 38921–9. doi: 10.1074/jbc.M206060200.

Song, L, Gao, S, Ye, B, Yang, M, Cheng, Y, Kang, D, Yi, F, Sun, J-P, Menéndez-Arias, L, and Neyts, J. 2024. Medicinal chemistry strategies towards the development of non-covalent SARS-CoV-2 Mpro inhibitors. *Acta Pharmaceutica Sinica B* **14**, 87–109. doi: 10.1016/j.apsb.2023.08.004.

Stofella, M, Grimaldi, A, Smit, JH, Claesen, J, Paci, E, and Sobott, F. 2024. Computational tools for hydrogen–deuterium exchange mass spectrometry data analysis. *Chemical Reviews* **124**, 12242–63. doi: 10.1021/acs.chemrev.4c00438.

Suárez, D, and Díaz, N. 2020. SARS-CoV-2 main protease: a molecular dynamics study. *Journal of chemical information and modeling* **60**, 5815–31. doi: 10.1021/acs.jcim.0c00575.

Sun, Z, Wang, L, Li, X, Fan, C, Xu, J, Shi, Z, Qiao, H, Lan, Z, Zhang, X, and Li, L. 2022. An extended conformation of SARS-CoV-2 main protease reveals allosteric targets. *Proceedings of the National Academy of Sciences* **119**, e2120913119. doi: 10.1073/pnas.2120913119.

Tao, X, Zhang, L, Du, L, Liao, R, Cai, H, Lu, K, Zhao, Z, Xie, Y, Wang, PH, Pan, JA, Zhang, Y, Li, G, Dai, J, Mao, ZW, and Xia, W. 2021. Allosteric inhibition of SARS-CoV-2 3CL protease by colloidal bismuth subcitrate. *Chem Sci* **12**, 14098–102. doi: 10.1039/d1sc03526f.

Thangaraj, SK, James, S, Rouvinen, J, and Jänis, J. 2019. Thermokinetic Analysis of Protein Subunit Exchange by Variable-Temperature Native Mass Spectrometry. *Biochemistry* **58**, 5025–29. doi: 10.1021/acs.biochem.9b00911.

Uetrecht, C, Watts, NR, Stahl, SJ, Wingfield, PT, Steven, AC, and Heck, AJ. 2010. Subunit exchange rates in Hepatitis B virus capsids are geometry- and temperature-dependent. *Phys Chem Chem Phys* **12**, 13368–71. doi: 10.1039/c0cp00692k.

Vuong, W, Khan, MB, Fischer, C, Arutyunova, E, Lamer, T, Shields, J, Saffran, HA, McKay, RT, van Belkum, MJ, and Joyce, MA. 2020. Feline coronavirus drug inhibits the main protease of SARS-CoV-2 and blocks virus replication. *Nature communications* **11**, 4282. doi: 10.1038/s41467-020-18096-2.

Yadav, R, Courouble, VV, Dey, SK, Harrison, JJE, Timm, J, Hopkins, JB, Slack, RL, Sarafianos, SG, Ruiz, FX, and Griffin, PR. 2022. Biochemical and structural insights into SARS-CoV-2 polyprotein processing by Mpro. *Science Advances* **8**, eadd2191. doi: 10.1126/sciadv.add2191. .

Yang, H, and Yang, J. 2021. A review of the latest research on M pro targeting SARS-COV inhibitors. *RSC medicinal chemistry* **12**, 1026–36. doi: 10.1039/d1md00066g.

Yang, H, Yang, M, Ding, Y, Liu, Y, Lou, Z, Zhou, Z, Sun, L, Mo, L, Ye, S, and Pang, H. 2003.

The crystal structures of severe acute respiratory syndrome virus main protease and its complex with an inhibitor. *Proceedings of the National Academy of Sciences* **100**, 13190–95. doi: 10.1073/pnas.1835675100.

Yang, Y, Ramelot, TA, Ni, S, McCarrick, RM, and Kennedy, MA. 2013. Measurement of rate constants for homodimer subunit exchange using double electron-electron resonance and paramagnetic relaxation enhancements. *J. Biomol. NMR* **55**, 47–58. doi: 10.1007/s10858-012-9685-7.

Zhang, L, Lin, D, Sun, X, Curth, U, Drosten, C, Sauerhering, L, Becker, S, Rox, K, and Hilgenfeld, R. 2020. Crystal structure of SARS-CoV-2 main protease provides a basis for design of improved α-ketoamide inhibitors. *Science* **368**, 409–12. doi: 10.1126/science.abb3405.

Zhang, Y, Guo, J, Liu, Y, Qu, Y, Li, Y-Q, Mu, Y, and Li, W. 2024. An allosteric mechanism for potent inhibition of SARS-CoV-2 main proteinase. *International Journal of Biological Macromolecules* **265**, 130644. doi: 10.1016/j.ijbiomac.2024.130644.

Zhao, Y, Fang, C, Zhang, Q, Zhang, R, Zhao, X, Duan, Y, Wang, H, Zhu, Y, Feng, L, and Zhao, J. 2022. Crystal structure of SARS-CoV-2 main protease in complex with protease inhibitor PF-07321332. *Protein & cell* **13**, 689–93. doi: 10.1007/s13238-021-00883-2.

Zhu, N, Zhang, D, Wang, W, Li, X, Yang, B, Song, J, Zhao, X, Huang, B, Shi, W, Lu, R, Niu, P, Zhan, F, Ma, X, Wang, D, Xu, W, Wu, G, Gao, GF, and Tan, W. 2020. A Novel Coronavirus from Patients with Pneumonia in China, 2019. *N Engl J Med* **382**, 727–33. doi: 10.1056/NEJMoa2001017.

Table 1. Inhibitors against SARS-CoV-2 M^{pro} and their inhibitory properties

Inhibitor	Binding site	Structure	EC_{50} (μM)	Hydrogen bonds	PDB ID	Reference
PF-07321332	active site	peptidomimetic	0.075	H41, G143, H164, E166, Q192	7VH8	(Owen *et al.*, 2021)
PF-00835231	active site	peptidomimetic	0.23	F140, H164, E166, Q189	6XHM	(Deshmukh et al., 2021)
GC376	active site	peptidomimetic	0.92	F140, G143, C145, H163, H164, E166	7D1M	(Vuong et al., 2020)
boceprevir	active site	peptidomimetic	15.57	H41, G143, H164, E166	7C6S	(Fu *et al.*, 2020)
carmofur	active site	non-peptidomimetic	24.3	G143, C145	7BUY	(Jin *et al.*, 2020b)
ebselen	active site	non-peptidomimetic	4.67	-	7BFB	(Amporndanai *et al.*, 2021)
MR6-31-2	active site	non-peptidomimetic	1.78	-	7BAL	(Amporndanai *et al.*, 2021)
AT7519	allosteric site	non-peptidomimetic	25.16	Q110, D153	7AGA	(Günther *et al.*, 2021)
pelitinib	allosteric site	non-peptidomimetic	1.25	-	7AXM	(Günther *et al.*, 2021)

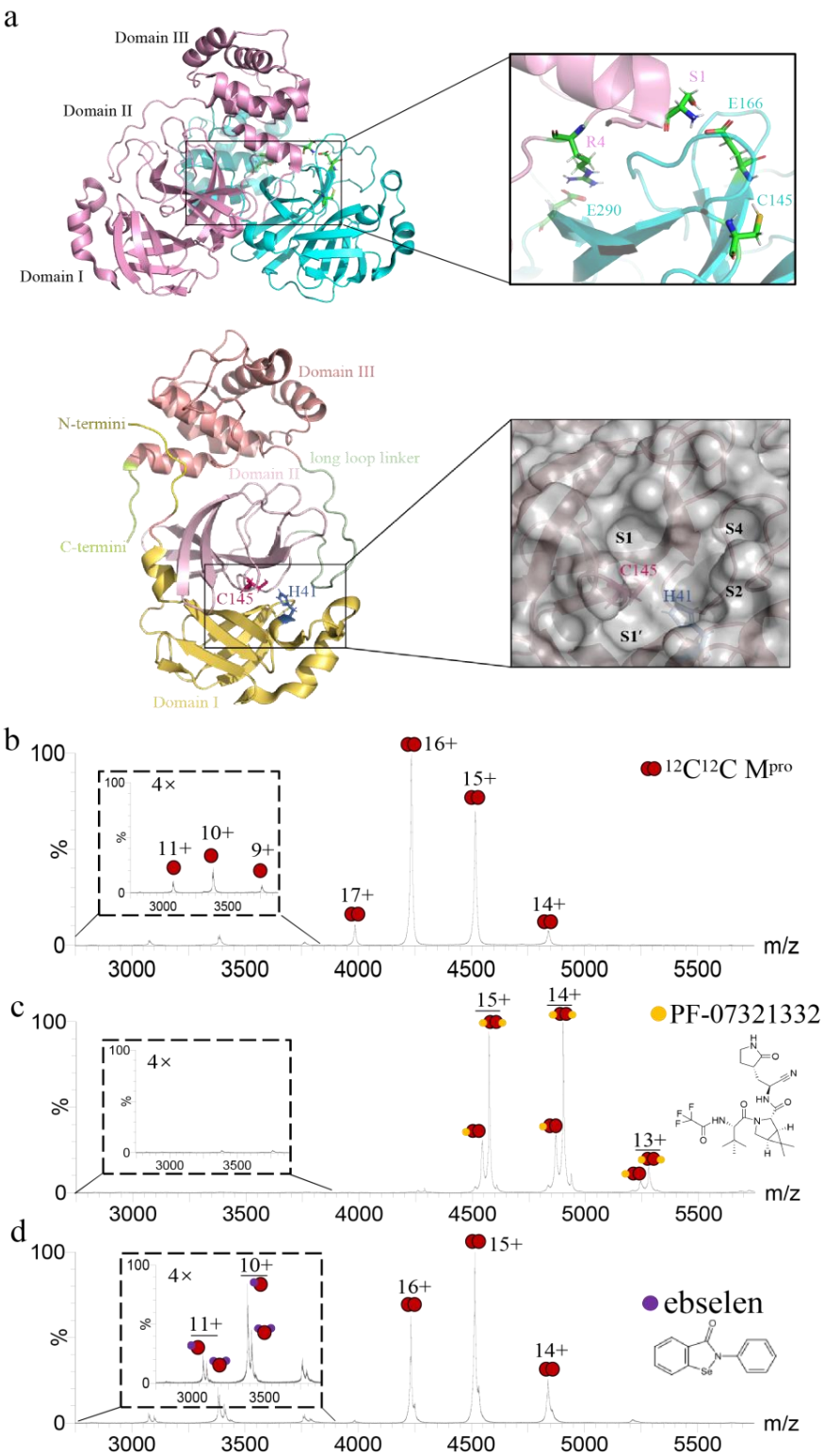

Figure 1. The monomer-dimer equilibrium modulation of M^{pro} induced by inhibitor binding. (a) Crystal structure of SARS-CoV-2 M^{pro} dimer, monomer, and active site pockets of SARS-CoV-2 M^{pro} with subsites and two catalytic dyad residues (H41 and C145) highlighted. (b) Native mass spectra of (b) unbound M^{pro}, (c) M^{pro}-PF-07321332 complex, and (d) M^{pro}-ebselen complex.

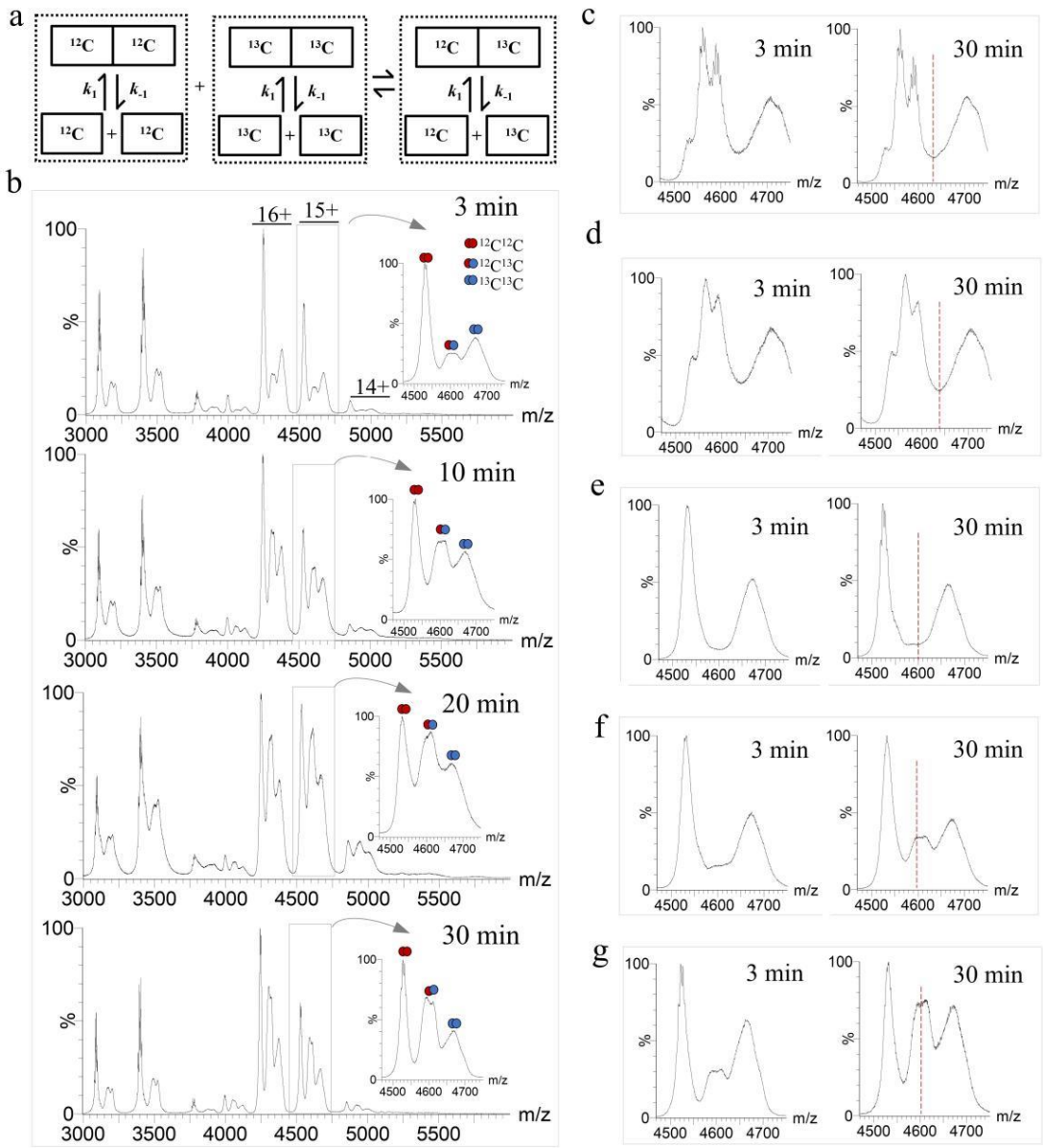

Figure 2. M^{pro} subunit exchange dynamics. (a) The strategy for M^{pro} subunit exchange. (b) Monitoring of unbound M^{pro} subunit exchange by native mass spectrometry. M^{pro} subunit exchange is affected by (c) PF-07321332, (d) PF-00835231, (e) GC376, (f) boceprevir, and (g) ebselen. The red dashed lines indicate the heterodimers.

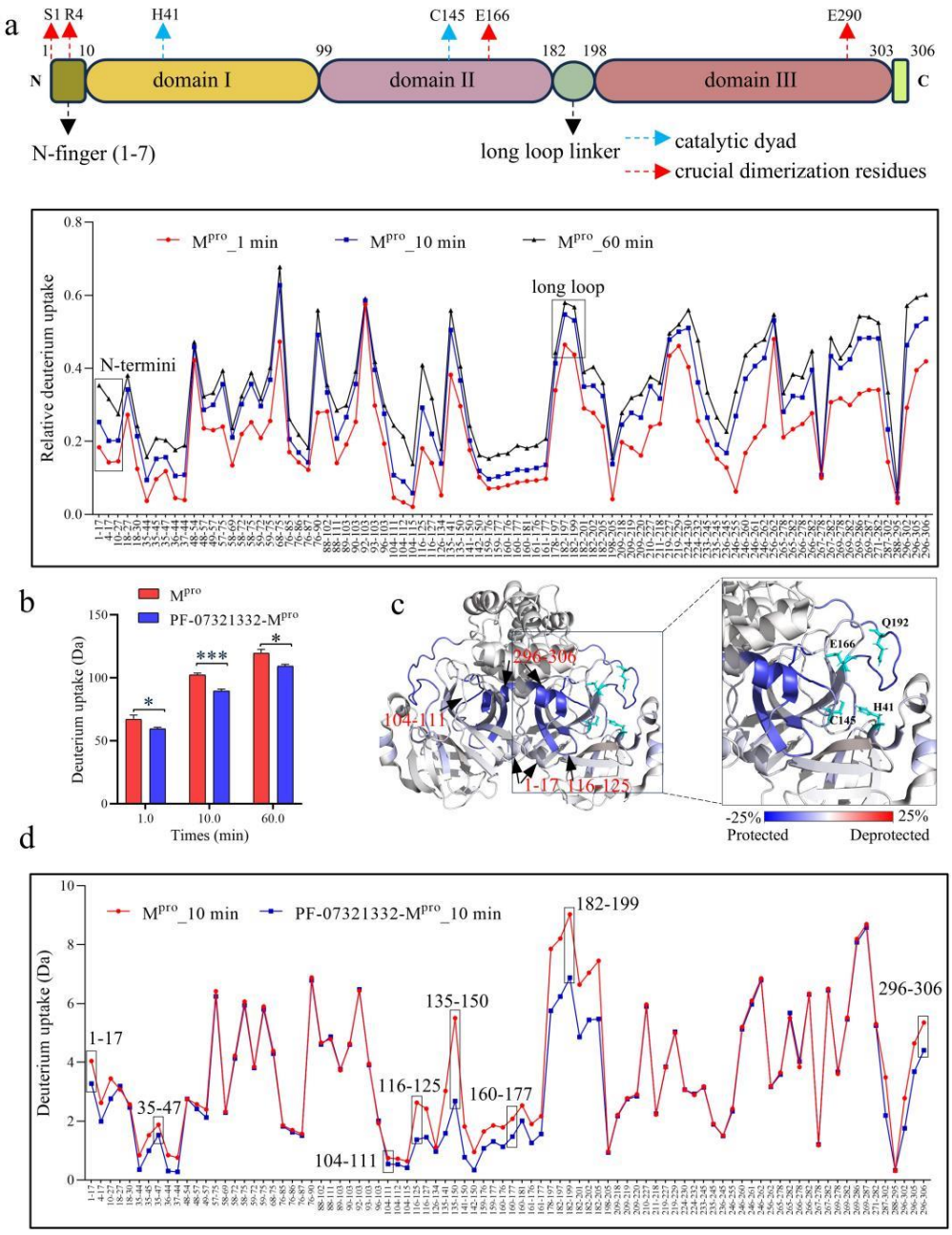

Figure 3. Conformational dynamics analysis of SARS-CoV-2 M^{pro} with PF-07321332. (a) The deuterium uptake plot for all identified peptides from M^{pro} at 1, 10, and 60 min. (b) Deuterium uptake of PF-07321332-bound M^{pro} by global HDX-MS. (c) The heat map of M^{pro} upon binding with PF-07321332 at 10 minutes was overlaid onto the crystal model of M^{pro} (PDB entry 7ALI). (d) The uptake line plots in the PF-07321332-bound M^{pro} at 10-min HDX labelling.

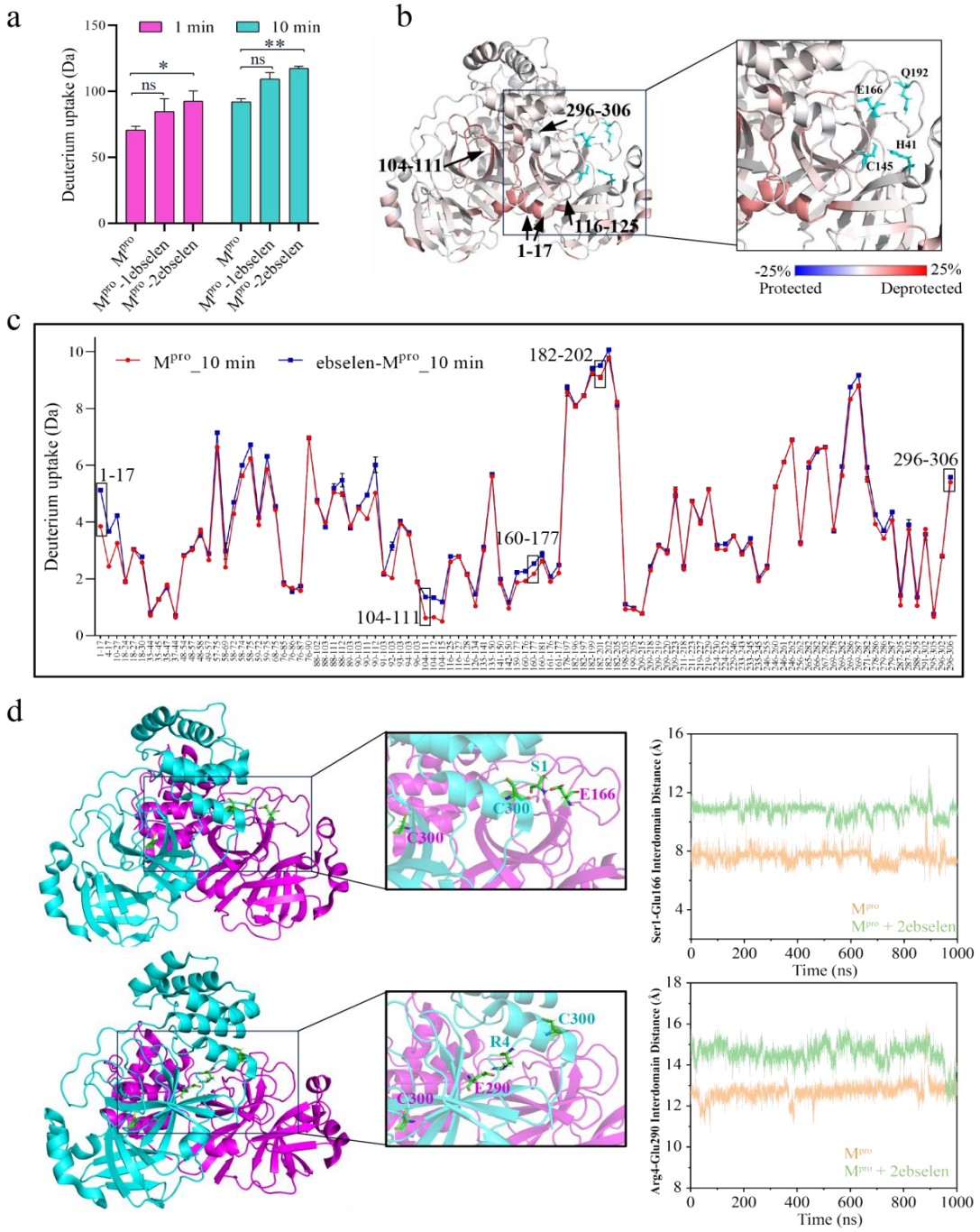

Figure 4. A new allosteric binding mode of ebselen on M^{pro}. (a) Deuterium uptake plot of ebselen-bound M^{pro} by global HDX-MS. (b) The heat map of M^{pro} upon binding with ebselen at 10 minutes was overlaid onto the crystal model of M^{pro} (PDB entry 7ALI). (c) The uptake line plots in the ebselen-bound M^{pro} at 10 minutes HDX labelling. (d) MD simulation of SARS-CoV-2 M^{pro} in the presence of ebselen on C300. Shifts in key intra-dimer interactions before and after covalent binding of ebselen at C300 on M^{pro}. Left panel: key amino acids involved in intra-dimer interactions are depicted on the crystal model of M^{pro} (PDB entry 7ALI). Right panel: the distances between R4 of one monomer and E290 of the other monomer Cα atoms, and residues S1 of one monomer and the other monomer E166 Cα atoms were measured, respectively.

858